Subarcsecond-resolution Imaging of M51 with the International LOFAR Telescope

Deepika Venkattu[1] , Peter Lundqvist[1] , Miguel Pérez Torres[2,3] , Leah Morabito[4,5] , Javier Moldón[2] , John Conway[6] ,
Poonam Chandra[7] , and Cyril Tasse[8,9]

[1] The Oskar Klein Centre, Department of Astronomy, Stockholm University, AlbaNova, SE-10691 Stockholm, Sweden; deepika.venkattu@astro.su.se
[2] Instituto de Astrofísica de Andalucía, Glorieta de la Astronomía, s/n, E-18008 Granada, Spain
[3] Facultad de Ciencias, Universidad de Zaragoza, Pedro Cerbuna 12, E-50009 Zaragoza, Spain
[4] Centre for Extragalactic Astronomy, Department of Physics, Durham University, Durham DH1 3LE, UK
[5] Institute for Computational Cosmology, Department of Physics, University of Durham, South Road, Durham DH1 3LE, UK
[6] Department of Space, Earth and Environment, Chalmers University of Technology, Onsala Space Observatory, SE-439 92 Onsala, Sweden
[7] National Radio Astronomy Observatory, 520 Edgemont Road, Charlottesville, VA 22903, USA
[8] GEPI & ORN, Observatoire de Paris, Université PSL, CNRS, 5 Place Jules Janssen, F-92190 Meudon, France
[9] Department of Physics & Electronics, Rhodes University, P.O. Box 94, Grahamstown, 6140, South Africa

Abstract

We present an International LOFAR Telescope (ILT) subarcsecond-resolution image of the nearby galaxy M51 with a beam size of $0\rlap{.}''436 \times 0\rlap{.}''366$ and rms of 46 μJy. We compare this image with a European VLBI Network study of M51 and discuss the supernovae in this galaxy, which have not yet been probed at these low radio frequencies. We find a flux density of 0.97 mJy for SN 2011dh in the ILT image, which is about five times smaller than the flux density reported by the LOFAR Two-metre Sky Survey (LoTSS) at $6''$ resolution using the same data set without the international stations. This difference makes evident the need for LOFAR international baselines to reliably obtain flux density measurements of compact objects in nearby galaxies. Our LOFAR flux density measurement of SN 2011dh directly translates into fitting the radio light curves for the supernova and constraining the mass-loss rates of the progenitor star. We do not detect two other supernovae in the same galaxy, SN 1994I and SN 2005cs, and our observations place limits on the evolution of both supernovae at radio wavelengths. We also discuss the radio emission from the center of M51, in which we detect the active galactic nucleus and other parts of the nuclear emission in the galaxy, with a possible detection of Component N. We discuss a few other sources, including the detection of a high-mass X-ray binary not detected by LoTSS but with a flux density in the ILT image that matches well with higher-frequency catalogs.

Unified Astronomy Thesaurus concepts: Radio continuum emission (1340); High angular resolution (2167); Galaxies (573); Core-collapse supernovae (304); Active galactic nuclei (16)

1. Introduction

The low-frequency radio sky is being extensively explored with instruments like the LOw Frequency ARray (LOFAR; van Haarlem et al. 2013), the Giant Metrewave Radio Telescope (GMRT; Intema et al. 2017), and the Very Large Array (VLA) Low Band Ionospheric and Transient Experiment (Polisensky et al. 2016). Along with the onset of the Square Kilometre Array era, there has never been a stronger focus on lower frequencies in the radio band. The most recent addition to this discovery space is the tested framework for subarcsecond-resolution imaging with the International LOFAR Telescope (ILT; Morabito et al. 2022). The ILT observations have proven to be very useful to unveil the nature of the radio-emitting sources in compact regions of nearby luminous infrared galaxies (e.g., detection of steep spectrum outflows, Varenius et al. 2016; Ramírez-Olivencia et al. 2018; probing thermal absorption in their nuclei, Ramírez-Olivencia et al. 2022), the complex structures in the radio lobes of active galactic nuclei (AGNs; Timmerman et al. 2022), the life cycle of radio galaxies (Kukreti et al. 2022), and much more. In this work, we present the first subarcsecond-resolution image of the nearby

galaxy M51, which resulted in the detection of 12 sources at 145 MHz.

The Whirlpool galaxy M51a (NGC 5194) is an almost face-on spiral galaxy with an interacting smaller companion, M51b (NGC 5195). At a distance of 8.4 Mpc (Vinkó et al. 2012), it has been extensively studied at various wavelengths and is a very good candidate for population studies. For example, Rampadarath et al. (2015) presented a radio survey of M51 with the European Very Long Baseline Interferometry (VLBI) Network (EVN) and discuss star formation, supernovae (SNe), and nuclear emission. Maddox et al. (2007) studied the compact sources in M51 with the VLA, complemented by multiwavelength data in the optical and X-ray. Radio emission remains unattenuated by dust and is hence an extinction-free tracer of star formation (Condon 1992). In addition, low-frequency radio observations are known to be primarily composed of synchrotron radiation with less than 10% of the continuum emission from thermal radiation (Tabatabaei et al. 2017).

In this context, a study of a nearby galaxy like M51 with the ILT is especially interesting because of the instrument's high angular resolution. With the inclusion of the international stations, the effective area of the beam is about a factor of 200 smaller than the beam area of the standard LOFAR surveys with the Dutch stations only. This huge improvement in resolution implies that compact sources can be more easily disentangled, and that ILT observations are essentially free from contamination from diffuse flux density.

Probing high-brightness compact sources within nearby galaxies, like SNe, SN remnants, AGNs, etc., with the ILT remains unexplored and could even lead to detections of new classes of compact objects. This study of M51 furnishes a proof of concept of this new discovery space. In the future, with automated processing of the ILT data of nearby galaxies, large populations of compact sources could be probed. For objects like radio SNe with longer emission periods at lower frequencies, along with the large sky coverage of LOFAR, this could mean a potential survey of all historical SNe in the galaxies surveyed by the ILT in the northern hemisphere in the near future. Since the radio luminosity of an SN also correlates with a higher progenitor wind density, the 150 MHz radio emission could help constrain different SN types with different progenitor stars from the mass-loss rates obtained.

We focus mostly on the low-frequency radio emission of the historic SNe detected in M51 as our chief interest, but we also briefly discuss the detection of the nucleus of M51, as this is the highest angular resolution observation of M51 in this frequency range. We again emphasize the aspect of the beam area provided by the ILT observations, which is similar to or even better than the resolution provided by world-class radio interferometers working at gigahertz frequencies, such as the VLA. This allows us to combine existing VLA observations (see Table 3) with ILT observations and determine the radio spectral energy distribution and light curve of these SNe in a meaningful way. This will involve a much greater degree of uncertainty if lower-resolution survey observations are used, as we discuss in Section 3.

The low-frequency radio emission from SNe is known to arise at later times than high frequencies, i.e., when the blast wave has propagated further away from the progenitor. It therefore probes mass loss at earlier times before the explosion, allowing, for instance, the detection of possible changes in mass loss prior to explosion. For radio SNe that have been studied extensively at higher radio frequencies, observing low-frequency spectral turnovers can help distinguish absorption models like free–free absorption (FFA) and synchrotron self-absorption (SSA), providing additional constraints on magnetic field strength and the wind properties of density and temperature.

In Section 2, we present the ILT observations and briefly describe the data reduction process for this. In Section 3, we present the detected sources and discuss our results with respect to previous work, with a focus on SNe and the nuclear emission in M51. Finally, Section 4 presents the conclusions.

2. Observations

2.1. LOFAR Observations

The LOFAR data are obtained from project LC2_038 (PI: H. Röttgering), observed on 2014 September 10 as a part of the LOFAR Two-metre Sky Survey (LoTSS; Shimwell et al. 2019). The second LoTSS data release (LoTSS-DR2; Shimwell et al. 2022) provides a mosaic of the pointing P39Hetdex19 from this project, with M51 close to the center. We successfully obtained an ILT image of the galaxy using the same data, which includes international stations but has not been included in the survey data product. This resulted in the first subarcsecond VLBI image of the galaxy M51 and an SN in it at frequencies as low as 145 MHz. The observation using the High Band Antenna (120–240 MHz) follows the standard strategy for LoTSS, which is a 10 minute observation of a bright flux density calibrator (3C 196 in this case) before and after the 8 hr on-source observation. Since this observation is from observation cycle 2 in 2014, only eight international stations are included: five in Germany (Effelsberg, Unterwei-lenbach, Tautenburg, Jülich, and Potsdam) and one each in the UK (Chilbolton), France (Nançay), and Sweden (Onsala). This is unlike the present day, where LOFAR routinely observes with 14 international stations, with more new stations being planned. The longest baseline length for this work is therefore 1297 km between the stations in France and Sweden (which yields an angular resolution of $0\rlap{.}''329$ at 145 MHz). The observation bandwidth is the standard survey frequency range of 120–168 MHz that avoids radio frequency interference above this frequency range. The data were recorded with 2 s sampling and in channels of 24.41 kHz width (8 channels per subband, 244 subbands).

The first part of the data reduction involves the use of PREFACTOR (https://github.com/lofar-astron/prefactor; Shim-well et al. 2019) for direction-independent calibration of the Dutch stations (core and remote). A model with suitably high resolution was used for 3C 196[10] in the PREFACTOR pipeline with CS001 as the reference station. All stations produced good solutions for total electron content and bandpass for both the calibrator and target.

The data were analyzed with v4.0.0 of the LOFAR-VLBI pipeline (Morabito et al. 2022 introduces the pipeline and describes v3.0.0). The latest version of the pipeline uses self-calibration optimized for LOFAR data (van Weeren et al. 2021) using NDPPP (van Diepen et al. 2018) and WSClean (Offringa et al. 2014). The pipeline uses the LoTSS and Long Baseline Calibrator Survey (LBCS; Jackson et al. 2016, 2022) catalog servers for useful information about the sources in our target field and nearby phase calibrators, respectively. The LBCS source L332164 (ILT J132703.36+470543.5), $0\rlap{.}°50803$ away, was used for an initial in-field correction of the phases and complex gains.

The pipeline forms a single superstation ST001 combining all of the core stations, which have already been phase-corrected using the PREFACTOR solutions. Unlike the pipeline described by Morabito et al. (2022), in the latest version, the delay calibration part of the pipeline is done by the facet self-calibration script in the form of three types of solutions done with the delay calibrator, which are then transferred onto the nearby target source (scalarphasediff, scalarphase, and scalarcomplexgain). The end products are a self-calibrated image of the delay calibrator along with an h5parm file of solutions to be transferred. These solutions are applied by the next part of the pipeline, which takes this solution-applied data set, phase shifts it to the target's coordinates, and splits off a smaller data set. Further self-calibration can be carried out if necessary. Since the target imaged here was the entire galaxy M51, in the last part of the pipeline, self-calibration of the target was not done. As a post-pipeline step, the reduced data set now centered on M51 was imaged using WSCLEAN (Offringa et al. 2014; Offringa & Smirnov 2017) with Briggs weighting parameters resulting in an image with a beam size of $0\rlap{.}''436 \times 0\rlap{.}''366$ and rms of 45.85 μJy.

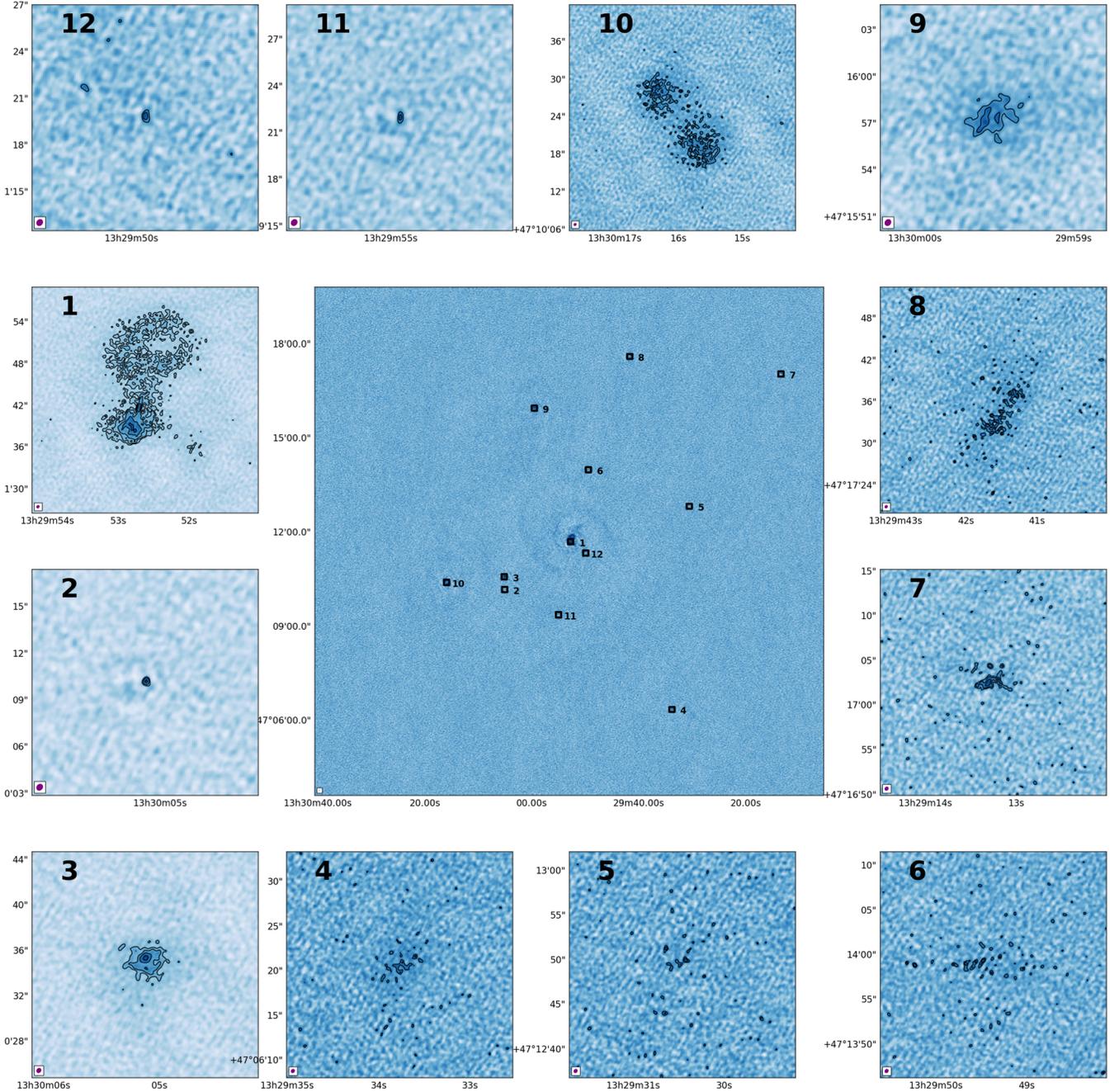[10] The 3C 196 model is courtesy of A. Offringa.

Figure 1. In the center is the ILT map of M51, with sources detected using PYBDSF marked in the same order as in Table 1. The panels on the side show the individual sources in greater detail. Sources of note are the nuclear emission in the center (1 is the position of the AGN) and SN 2011dh (2).

After imaging the galaxy this way using the reduced data set from the pipeline that includes the superstation ST001, imaging was also performed using a modified data set that included the core stations instead of the combined superstation, with Briggs weighting parameters and a minimum *uv* cut of 5 kλ in order to filter out some of the diffuse emission and mimic the presence of the superstation. This resulted in an image with a much lower noise (24.05 μJy) but a larger beam size (0.″561, 0.″475) and hence lower resolution and significantly more negative bowl effects than the image with the superstation. Hence, throughout this paper, we only use the higher-resolution image with ST001 for all purposes, including source detection and flux estimation.

2.2. Source Detection

Figure 1 (center panel) shows the ILT image of M51. Source detection was performed on this image using PYBDSF (Mohan & Rafferty 2015). To enable extended sources to be detected (especially in the center of M51a), we set the control PYBDSF parameters `flag_maxsize_bm=100` and `rms_map=False` while maintaining the threshold for island detection at 6σ. A more detailed discussion of detecting extended sources is given in the PYBDSF documentation (https://pybdsf.readthedocs.io/en/latest/index.html). In total, 12 distinct sources were identified in the ILT image by PYBDSF (see Table 1 and the side panels of Figure 1). Two of these sources are identified by PYBDSF as having subcomponents, with properties as listed in

Table 1
Sources Detected in M51 with the ILT at 145 MHz

No.	Source/ Subcomponent Name	Position (J2000.0) R.A. 13 h	Decl. 47 d	Flux (mJy)	PYBDSF Size Major (arcsec)	Minor (arcsec)	Cross-identification LoTSS	NED
1	J132952+471142	29m52.62 s	11m42.83 s	0.46 ± 0.3	1.32 ± 0.86	0.87 ± 0.5	ILT J132952.71+471143.3	Messier 051a (center)
2	J133005+471010	30m05.09 s	10m10.17 s	0.97 ± 0.14	0.699 ± 0.08	0.479 ± 0.04	ILT J133005.07+471011.0	SN 2011dh
3	J133005+471035	30m05.12 s	10m34.77 s	71.91 ± 2.5	3.31 ± 0.19	2.8 ± 0.16	ILT J133005.03+471035.2	2CXO J133005.0+471035
4	J132933+470620	29m33.76 s	06m20.70 s	12.71 ± 1.73	6.95 ± 0.95	4.12 ± 0.56	ILT J132933.78+470621.3	WISEA J132933.76+470621.4
5	J132930+471250	29m30.45 s	12m49.50 s	12.95 ± 2.17	7.56 ± 1.27	5.94 ± 0.99	ILT J132930.46+471250.8	SSTSL2 J132930.49+471250.5
6	J132949+471358	29m49.36 s	13m58.90 s	11.34 ± 2.33	5.97 ± 1.78	2.78 ± 0.81	ILT J132949.59+471359.2	Messier 051:[MCK2007] 014
7	J132913+471702	29m13.24 s	17m02.50 s	10.39 ± 1.45	2.56 ± 0.46	1.34 ± 0.23	ILT J132913.38+471703.9	ILT J132913.3+471704.7
8a	J132941+471736	29m41.38 s	17m36.70 s	20.17 ± 2.17	3.39 ± 0.66	2.83 ± 0.54	ILT J132941.60+471736.2	SSTSL2 J132941.50+471734.9
8b	J132941+471732	29m41.60 s	17m32.40 s	16.16 ± 1.56	5.74 ± 0.55	4.04 ± 0.39	”	”
9	J132959+471557	29m59.50 s	15m57.40 s	56.44 ± 2.46	2.94 ± 0.24	2.14 ± 0.17	ILT J132959.89+471549.1	Messier 051b
10a	J133016+471027	30m16.30 s	10m27.70 s	60.62 ± 2.55	8.82 ± 0.37	6.96 ± 0.29	ILT J133015.94+471023.9	2CXO J133016.0+471024
10b	J133015+471019	30m15.68 s	10m19.40 s	81.56 ± 2.97	10.28 ± 0.37	8.13 ± 0.3	”	”
11	J132954+470922	29m54.94 s	09m22.00 s	0.83 ± 0.17	0.91 ± 0.16	0.49 ± 0.06	⋯	CXOU J132954.9+470922
12	J132949+471119	29m49.91 s	11m19.85 s	0.95 ± 0.20	0.90 ± 0.17	0.60 ± 0.09	⋯	2CXO J132949.9+471120

Note. The image rms is 46 μJy beam^{-1}. The same value applies for the localized island rms detected by PYBDSF for fitting Gaussians. The error in the flux density column is the error from PYBDSF fitting.
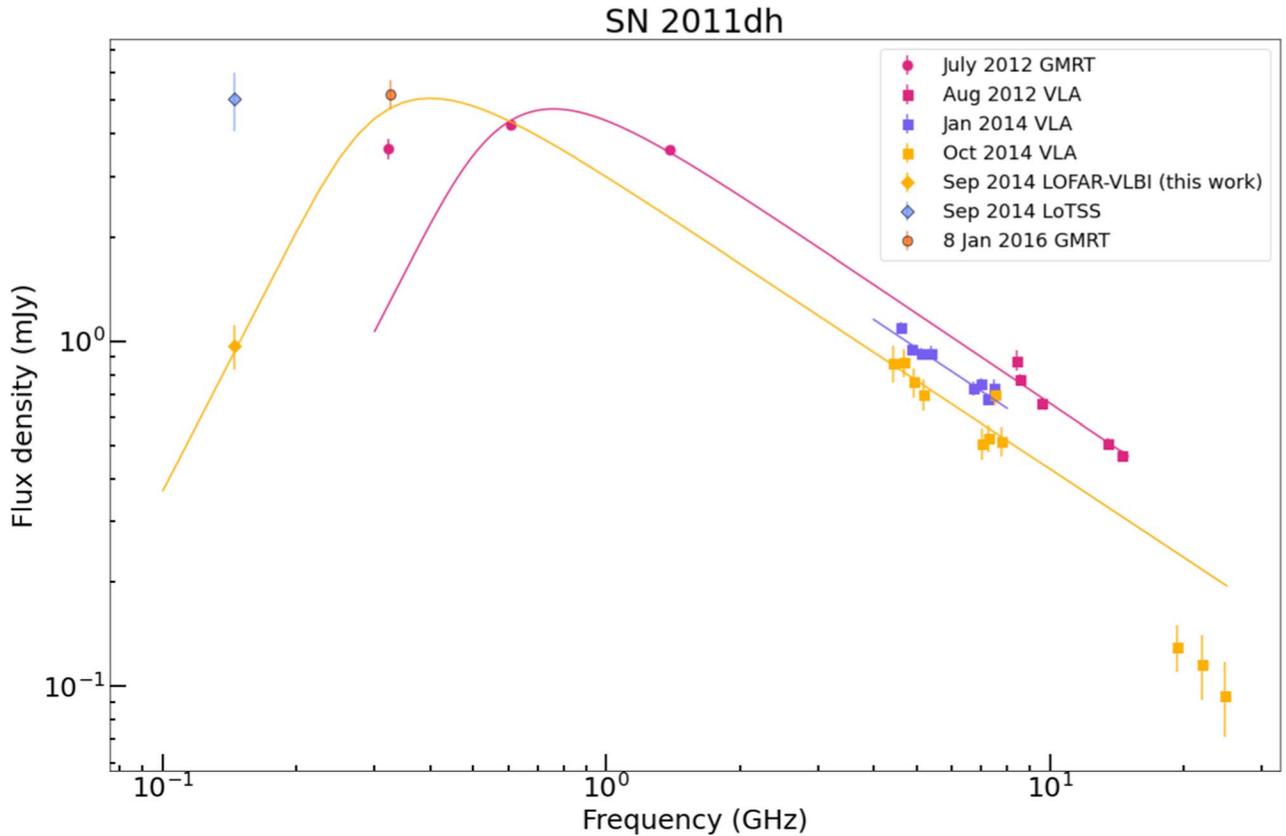
Figure 2. Radio spectra of SN 2011dh at three different distinct epochs using the VLA, GMRT, and ILT data in Table 3. The same color is used to denote data considered as one epoch and included in a single fit, for example, 2014 September LOFAR-VLBI and 2014 October VLA observations of SN 2011dh. Data not included in the analysis have translucent markers; for example, data from the LoTSS catalog at 6″ resolution are plotted to show the difference in flux densities. See text and Figure 3 for further details.

Table 1 (sources 8 and 10 listed with their subcomponents). In order to compare the number of source detections and flux densities between our subarcsecond-resolution ILT image and the 6″ resolution LoTSS survey, we searched for cross-identified sources in the LoTSS catalog that lay within a 2″5 radius of each LOFAR-VLBI source, resulting in 10 associated LoTSS detections. One source (source 11, named J132954 +470922 in Table 1), although detected above 6σ in the ILT image, is not detected in the LoTSS catalog. PYBDSF also predicts possible sources in the spiral arms of the galaxy, but since this area has only extended emission and no cross-matches, we do not take these into account any further. We also compare our PYBDSF catalog with the SN remnant candidates discussed in Winkler et al. (2021), especially the 16 radio sources that are also detected by Maddox et al. (2007). Of these, we have a possible cross-match for only one, which is listed as source 17 in Maddox et al. (2007) and is the last source in Table 1 of this work, which is also not detected in the LoTSS catalog.

3. Results

3.1. Supernovae

Currently, four SNe have been detected in the M51 system: Type Ia SN 1945A (Kowal & Sargent 1971), Type Ib/c SN 1994I (Puckett et al. 1994), Type IIP SN 2005cs (Kloehr et al. 2005), and Type IIb SN 2011dh (Griga et al. 2011), of which radio emission has been detected for SN 1994I (e.g., Weiler et al. 2011) and SN 2011dh (e.g., Krauss et al. 2012; Horesh

et al. 2013). Only one SN is detected with LOFAR (SN 2011dh is visible in both LoTSS and our ILT image), and in this section, we discuss SN 2011dh and constrain the radio emission from the other core-collapse SNe with upper limits from the ILT image, which in turn constrains the SN–circumstellar matter interaction properties.

3.1.1. SN 2011dh

3.1.2. SN 2011dh Ancillary Data

Object SN 2011dh is detected in both the LoTSS and ILT images. The ILT observation is discussed in Section 2, and the PYBDSF fit for SN 2011dh from the ILT image can be found in Table 1 (source 2). Both the LoTSS and ILT flux densities for the SN are shown in Figure 2. To complement the LOFAR data of SN 2011dh, we consider other late-time radio observations of the SN here.

GMRT observations. The GMRT data from 2012 July published in Yadav et al. (2016) are used in this work to complement the VLA data at a similar epoch from 2012 August. Roy & Manna (2021) studied seven nearby galaxies with the GMRT, including M51. The flux for SN 2011dh, clearly visible in the radio map of the galaxy, is also used in this work (S. Roy 2021, private communication). This gives an idea of the SN at a much later epoch at lower frequencies.

VLA observations. The VLA data used for this work were from VLA programs 12A-286, 13A-370, and 14B-479 (data taken on 2012 August 1, 2014 January 31, and 2014 October
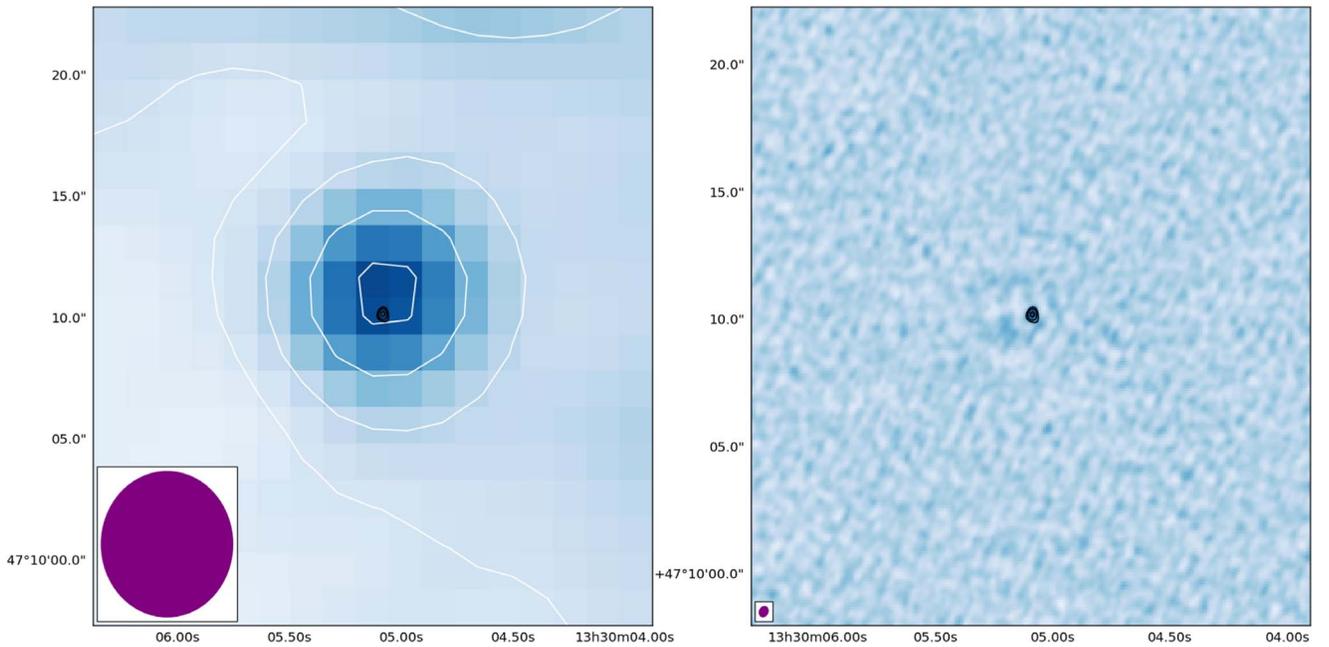
Figure 3. Left: ILT image in black contours overlaid on the LoTSS-DR2 image with white contours. Contours are from 4σ to 5σ for the ILT and start from 1σ to 5σ for LoTSS. Right: ILT image in background with black contours overlaid and a linear stretch from -5σ to $+5\sigma$. The restoring beams for the two LOFAR images are shown in the bottom left corners (LoTSS: $6''$; ILT: $0''.44 \times 0''.37$).

Table 2
SSA Model Fits—SN 2011dh

Day	S_{ν_τ} (mJy)	ν_τ (GHz)	R_s (10^{16} cm)	B_s (G)	A_*
497	4.53 ± 0.06	0.64 ± 0.01	4.04 ± 0.29	0.08 ± 0.002	9.6 ± 0.5
1197	4.75 ± 1.77	0.34 ± 0.05	7.9 ± 1.7	0.04 ± 0.01	22 ± 6

Note. Parameters estimated from an SSA fit to the observed radio spectrum of SN 2011dh (source 2 in Table 1). In the fits, we have assumed a filling factor $f = 0.5$ and $\epsilon_B = \epsilon_e = 0.1$. See text for further details.

18, respectively; Kundu et al. 2019). We reanalyzed the VLA radio data for SN 2011dh of 2014 January 31 and 2014 October 18 presented and used in Kundu et al. (2019). For these two epochs, we find a notably higher flux, around a factor of 5–15, more in line with the results of de Witt et al. (2016). We suspect that there could have been a problem with the CASA version 4.3.1 pipeline used in Kundu et al. (2019). With these new estimates of the flux densities on 2014 January 31 and 2014 October 18, the results of Kundu et al. (2019) are valid for up to around 500 days after the explosion of the SN.

3.1.3. SN 2011dh Modeling

The Type IIb SN 2011dh was first detected by Griga et al. (2011). Figure 2 shows the light curve with the 2012 epoch in magenta, the 2014 January epoch in purple, and the 2014 September epoch in yellow. The VLA data are denoted by squares, GMRT data by circles, and LOFAR data by diamonds. The LoTSS data point (5.2 ± 0.9 mJy) is also plotted for comparison with the ILT data point, showing a large discrepancy in flux densities with the LoTSS value more than five times higher. This arises from the larger beam size of LoTSS that does not include the international stations. The higher-resolution observation with a lower beam size is not as contaminated by diffuse emission from the surrounding region,

and this translates directly into estimating parameters such as the mass-loss rates of the progenitor of SN 2011dh. We note here that the LoTSS catalog has a PYBDSF fit for SN 2011dh that is bigger than its beam size of $6''$ ($8''.05 \times 7''.51$) and shows a peak flux of 3.1 ± 0.4 mJy. It is likely then that the bias due to the diffuse flux from the background would be lower when considering the peak flux, rather than the total flux from the LoTSS catalog, which is fit for a region much larger than the beam size. There is also a GMRT flux density value from 2016. Figure 3 shows the ILT and LoTSS images of SN 2011dh. The curves are fit to the data using EMCEE (Foreman-Mackey et al. 2013) with an SSA model,

$$ S(\nu) = 1.582\, S_{\nu_\tau} \left(\frac{\nu}{\nu_\tau} \right)^{5/2} \left\{ 1 - \exp\left[-\left(\frac{\nu}{\nu_\tau} \right)^{-(p+4)/2} \right] \right\}, \quad (1) $$

where S_{ν_τ} is the flux density for SSA optical depth unity, and ν_τ is the frequency at which this occurs. For this model, Krauss et al. (2012) found a value of $p = 2.8$ and an observed peak radio flux density at $\nu_{\rm op} = 1.17\nu_\tau$. We find values of $p = 2.74$ and 2.71 and observed peak radio flux densities occurring at $\nu_{\rm op} = 1.178\nu_\tau$ and $1.184\nu_\tau$ for the 2012 and 2014 epochs, respectively. The values for the fit parameters are shown in Table 2.

The synchrotron emission is assumed to arise as a result of the interaction of the SN ejecta with circumstellar matter, and the fit parameters can be used to estimate some other important parameters, namely,

$$R_s = 3.9 \times 10^{14} \, \alpha^{-1/19} \left(\frac{f}{0.5}\right)^{-1/19} \left(\frac{D}{\text{Mpc}}\right)^{18/19}$$

$$\times \left(\frac{S_{\nu_{\text{op}}}}{\text{mJy}}\right)^{9/19} \left(\frac{\nu_{\text{op}}}{5 \text{ GHz}}\right)^{-1} \text{cm}, \quad (2)$$

$$B_s = 1.0 \, \alpha^{-4/19} \left(\frac{f}{0.5}\right)^{-4/19} \left(\frac{D}{\text{Mpc}}\right)^{-4/19}$$

$$\times \left(\frac{S_{\nu_{\text{op}}}}{\text{mJy}}\right)^{-2/19} \left(\frac{\nu_{\text{op}}}{5 \text{ GHz}}\right) \text{G}, \quad (3)$$

and

$$A_* = 0.82 \, \alpha^{-8/19} \left(\frac{\epsilon_B}{0.1}\right)^{-1} \left(\frac{f}{0.5}\right)^{-8/19} \left(\frac{D}{\text{Mpc}}\right)^{-8/19}$$

$$\times \left(\frac{S_{\nu_{\text{op}}}}{\text{mJy}}\right)^{-4/19} \left(\frac{\nu_{\text{op}}}{5 \text{ GHz}}\right)^2 \left(\frac{t}{10 \text{ days}}\right)^2. \quad (4)$$

Here R_s is the radius of the forward shock advancing into the circumstellar medium, f is the filling factor of the shocked gas that emits synchrotron emission, and D is the distance to the SN, for which we adopt 8.4 ± 0.6 Mpc (Vinkó et al. 2012). Furthermore, B_s is the magnetic field strength of the shocked circumstellar gas, ϵ_B is the fraction of the forward shock energy that goes into the magnetic field energy density, and α is the ratio of the fraction of the forward shock energy that goes into the energy density of relativistic electrons (ϵ_e) to ϵ_B. Here A_* measures the density of the circumstellar gas such that $\rho_w = 5 \times 10^{11} A_* r^{-2}$ g cm^{-3} and therefore corresponds to a mass-loss rate in units of $10^{-7}(v_w/10 \text{ km s}^{-1})^{-1}$ $M_\odot$ yr^{-1} assuming the circumstellar gas arises from steady mass loss from the progenitor with the wind speed v_w. We can estimate the retardation of the circumstellar shock assuming $R_s \propto t^m$ with values taken from Table 2, and we find $m = 0.76 \pm 0.26$, which is consistent with the $m = 0.87 \pm 0.07$ found by Krauss et al. (2012) for the first ~100 days of evolution. We also note that the density profile of the ejecta in the hydrodynamical model of Kundu et al. (2019) is roughly $\rho \propto r^{-6}$ for the ejecta that are traversed by the reverse shock during the first few years. For a constant mass-loss rate characterizing the wind, $m = (n-3)/(n-2)$ (n being the index of the density slope of the ejecta). This means that $m \sim 0.75$ in the hydrodynamical models by Kundu et al. (2019). For the magnetic field strength, we obtain $B_s \propto t^q$, where $q = -0.74 \pm 0.16$, which means that B_s is inversely proportional to R_s, as has been assumed to be the general case in previous modeling (e.g., Chevalier & Fransson 2017).

For $v_w = 1000$ km s^{-1}, we find a mass-loss rate of $(9.6 \pm 0.5) \times 10^{-5}$ $M_\odot$ yr^{-1}, and for a wind velocity of 20 km s^{-1}, $(1.9 \pm 0.1) \times 10^{-6}$ $M_\odot$ yr^{-1} for the 2012 epoch. For the 2014 epoch, we find mass-loss rates of $(2.2 \pm 0.6) \times 10^{-4}$ $M_\odot$ yr^{-1} for a wind velocity of 1000 km s^{-1} and $(4.4 \pm 1.2) \times 10^{-6}$ $M_\odot$ yr^{-1} for a wind velocity of 20 km s^{-1}. These numbers are ~2.7 (6)

(for 497 and 1197 days, respectively) times higher than estimated by Krauss et al. (2012) for the early phase but smaller than the $A_* = 40$ by Kundu et al. (2019), who, however, used the values $\epsilon_B = 0.04$ and $\epsilon_e = 0.03$, which are lower than our $\epsilon_B = \epsilon_e = 0.1$. If we use their values for ϵ_B and ϵ_e, we get ~2.8 times larger A_* values than those in Table 2 (since $\dot{M} \propto \alpha^{-8/19} \epsilon_B^{-1}$) and consistent with Kundu et al. (2019). A caveat is that Kundu et al. (2019) used too-low observed fluxes (cf. above), which should mean that their estimate of $\dot{M}$ should still be higher than ours. Regardless of that, the mass-loss rate of the progenitor may have been higher earlier in the evolution of the progenitor than just prior to the explosion, or there may have been a change in one or both of the ϵ parameters as the circumstellar shock evolved.

3.1.4. SN 1994I

Object SN 1994I is a Type Ib/c SN first detected by Puckett et al. (1994). For our assumption of 8.4 Mpc, following the expansion of SN 1994I derived by Weiler et al. (2011), we find $1.38(t_{\text{age}}/1d)$ μas. This gives a size of 10.3 mas for SN 1994I at the time of our observation with LOFAR (7466 days).

Maddox et al. (2007) detected SN 1994I with the VLA almost a decade after explosion in two different frequency bands and derived a spectral index of −1.04. Scaling the data at 1.4 GHz to 145 MHz using optically thin synchrotron emission scaling, $S_{0.145}/S_{1.4} = (0.145/1.4)^{-1.04}$, we get a flux of 1.69 mJy at 2927 days. With this scaled flux at 2927 days and using the light-curve model in Weiler et al. (2011), where the flux density decreases with time following $S \propto t_{\text{age}}^\beta$, and $\beta = -1.42$, we estimate a flux of 0.46 mJy at the ILT observation of 7466 days. Our detection threshold is 0.23 mJy, and given that the SN was beginning to fade in the 6 cm observations a decade before our observations, it is likely that it has entered a region with less mass loss in the wind, or it could be due to a weakening of the reverse shock if it has entered a flatter density profile of the ejecta, as may have been the case for SN 1993J (Björnsson 2015; Kundu et al. 2019).

3.1.5. SN 2005cs

Discovered by Kloehr et al. (2005) on 2005 June 28.9, SN 2005cs was found to be a relatively underluminous Type II plateau (Type IIP) SN, classified by Pastorello et al. (2006) as low luminosity, or LL Type IIP. The SN was observed in the radio shortly after the explosion but not detected (Stockdale et al. 2005). We have included those 3σ upper limits, as well as our upper limit from the ILT image, in Table 3 and Figure 4.

A recent attempt by Kozyreva et al. (2022) to model the optical light curves for SN 2005cs, as well as another LL Type IIP, SN 2020cxd, showed an explosion energy of $E = 7 \times 10^{49}$ erg and ejecta mass of $M = 7.4 \, M_\odot$ (their model s9.0 provided good fits). The explosion simulation was made in 3D and indicated strong asymmetry of the ejecta, but Kozyreva et al. (2022) also made spherically symmetric averages of s9.0, which we have used as a guide for our modeling of the radio data. We simplify the ejecta structure further by assuming that the ejecta are homologous and consist of an inner structure with a density profile $\rho_i \propto V^{-a}$ and an outer structure with $\rho_o \propto V^{-n}$. The break in density structure then occurs at the velocity

$$V_{\text{b}} = \sqrt{\frac{2E}{M} \frac{(n-5)(5-a)}{(n-3)(3-a)}}, \quad (5)$$

Table 3
Parameters of SNe 1994I, 2005cs, and 2011dh

SN	Date of Observation (UT)	Time after Explosion (days)	Central Frequency (GHz)	Flux Density (μJy)	Luminosity (10^{25} erg s^{-1} Hz^{-1})	References
SN 1994I	2004 Jan 5	3567.00	1.425	160 ± 22	1.35 ± 0.19	1
	2004 Jan 5	3567.00	4.860	46 ± 11	0.39 ± 0.09	1
	2011 Nov 7	6428.00	1.65	<50	<0.42	2
	2014 Sep 10	7466.00	0.145	<138	<1.17	3
SN 2005cs	2005 Jul 2.01	4.51	22.64	<585	<4.94	4
	2005 Jul 3.00	5.50	8.460	<189	<1.60	4
			14.94	<900	<7.60	4
	2005 Jul 8.97	11.47	8.460	<291	<2.46	4
			22.64	<918	<7.75	4
	2005 Jul 22.04	24.54	8.460	<161	<1.36	4
			22.64	<464	<3.92	4
	2005 Aug 9.00	42.50	8.460	<129	<1.09	4
			14,94	<187	<1.58	4
			22.64	<372	<3.14	4
	2014 Sep 10	3361.5	0.145	<138	<1.17	3
SN 2011dh	2012 Jul 20	415	0.323	3610 ± 250	30.5 ± 2.1	5
	2012 Jul 21	416	0.607	4240 ± 70	35.8 ± 0.6	5
	2012 Jul 26	421	1.387	3600 ± 50	30.4 ± 0.4	5
	2012 Aug 1	427	8.4	880 ± 60	7.4 ± 0.5	3
			8.55	778 ± 24	6.6 ± 0.2	3
			9.56	663 ± 23	5.6 ± 0.2	3
			13.5	507 ± 17	4.3 ± 0.1	3
			14.5	466 ± 17	3.9 ± 0.1	3
	2014 Jan 31	975	4.615	1099 ± 43	9.2 ± 0.4	3
			4.871	949 ± 29	8.0 ± 0.2	3
			5.127	925 ± 30	7.8 ± 0.2	3
			5.383	926 ± 42	7.8 ± 0.3	3
			6.715	731 ± 34	6.2 ± 0.3	3
			6.971	754 ± 26	6.4 ± 0.2	3
			7.227	679 ± 29	5.7 ± 0.2	3
			7.483	731 ± 46	6.2 ± 0.4	3
	2014 Sep 10	1197	0.145	5200 ± 900	43.9 ± 7.6	6
			0.145	970 ± 140	8.19 ± 1.18	3
	2014 Oct 18	1235	4.415	866 ± 106	7.3 ± 0.9	3
			4.671	869 ± 83	7.3 ± 0.7	3
			4.927	762 ± 74	6.4 ± 0.6	3
			5.183	703 ± 73	5.9 ± 0.6	3
			7.015	507 ± 54	4.3 ± 0.4	3
			7.271	524 ± 48	4.4 ± 0.4	3
			7.527	703 ± 51	5.9 ± 0.4	3
			7.783	515 ± 50	4.3 ± 0.4	3
			19.315	130 ± 20	1.1 ± 0.2	3
			21.997	116 ± 25	9.8 ± 0.2	3
			24.681	94 ± 23	0.8 ± 0.2	3
	2016 Jan 8	1682	0.325	5200 ± 500	43.9 ± 4.2	7

Notes. The columns starting from left to right are as follows: SN name; date of observation; time after explosion, where UT 2005 June 27.5 has been used as the explosion date for SN 2005cs (Pastorello et al. 2006) and UT 1994 March 31 has been used as the explosion date for SN 1994I (Weiler et al. 2011); central frequency of observation; flux densities and 3σ upper limit on the same; and luminosity and 3σ upper limit on the same. References: (1) Maddox et al. (2007); (2) Rampadarath et al. (2015); (3) this work; (4) Stockdale et al. (2005); (5) Yadav et al. (2016); (6) LoTSS catalog at 6″ resolution; (7) private communication, S. Roy.

which, for the parameters of the s9.0 model, results in a break in the range of $(0.98-1.25) \times 10^3$ km s^{-1} for $a \in [0, 1]$ and $n \in [8, 14]$. In the angle-averaged s9.0 model, a break in velocity of at least 800 km s^{-1} occurs, and $a \sim 0$ close to 3 days after explosion. These velocities agree with the photospheric velocity for s9.0 around 100–120 days, which is also just before the observed light-curve drop for SN 2005cs. To set the transition between the outermost ejecta and circumstellar

medium, we assume that the progenitor had a constant $\dot{M}/v_w$, where $\dot{M}$ is the mass-loss rate, and v_w is the wind speed. This gives a density dependence for the circumstellar medium, which is $\rho_w \propto r^{-2}$. We further use the information that the maximum ejecta velocity at early epochs may be as high as 1.2×10^4 km s^{-1} (Pastorello et al. 2006). The ratio $\dot{M}/v_w$ is then found from setting $\rho_o = \rho_w$ at the radius 3.1×10^{14} cm, which is the distance the outermost ejecta have reached at
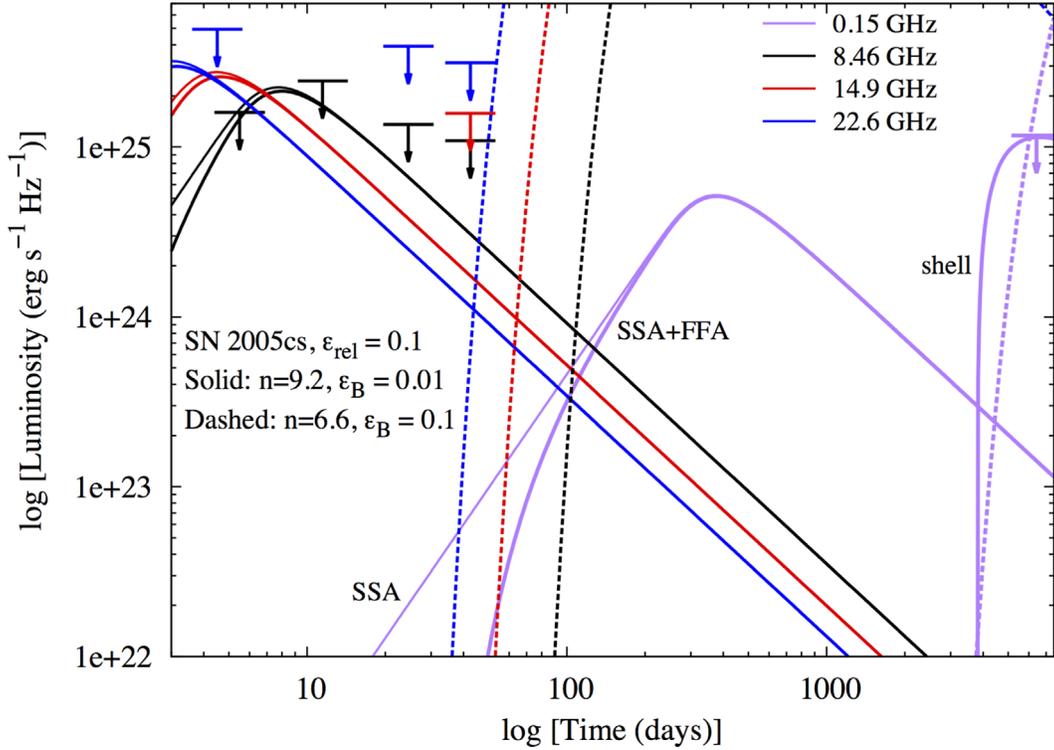
Figure 4. Radio modeling of SN 2005cs. For the solid lines, we have used the parameters $n = 9.2$, $\epsilon_B = 0.01$, and $\epsilon_e = 0.1$. The mass-loss rate for the wind case is $\dot{M} = 5 \times 10^{-7}(v_w/10\,\mathrm{km\,s^{-1}})^{-1}\,M_\odot\,\mathrm{yr}^{-1}$, whereas for the shell case, it is lower inside and $\sim$three times larger outside 4×10^{17} cm. The dashed lines are for a model with $n = 6.6$, $\epsilon_B = 0.1$, $\epsilon_e = 0.1$, and $\dot{M} = 8.5 \times 10^{-5}(v_w/10\,\mathrm{km\,s^{-1}})^{-1}\,M_\odot\,\mathrm{yr}^{-1}$. See text for further details and Table 3 for the data in the plot. The ILT data from this work are labeled as 0.15 GHz.

3 days. We find that these requirements indicate that $\dot{M} < 6.0 \times 10^{-6}(v_w/10\,\mathrm{km\,s^{-1}})^{-1}\,M_\odot\,\mathrm{yr}^{-1}$ for $n \geqslant 8$ and $a \in [0, 1]$.

To further limit the likely value of n, we use the estimated electron-scattering optical depth $\tau_e \sim 2/3$ through the outermost ejecta. Kozyreva et al. (2022) estimated that the velocity at which this occurs is positioned close to the photosphere for the first $\sim$20 days. At 20 days, this ejecta velocity is $\sim$2000 km s^{-1}. In our models, assuming fully ionized ejecta consisting of hydrogen and helium with a ratio of He/H $= 0.1$, $\tau_e(20\,\mathrm{days}) \geqslant 1$ through ejecta with velocities $>$2000 km s^{-1} for $a \in [0, 1]$ and $n < 15$. However, an electron fraction of $\sim$0.2 may be more likely (e.g., Ergon & Fransson 2022), which in our case limits n to the range $n \in [9, 14]$, but to allow for even lower electron fractions, we also include $n = 8$. Guided by these estimates, and since models with $a = 0$ and 1 do not differ to any larger extent, we will concentrate on models with $n \in [8, 14]$ and $a = 0$. The mass-loss rates for these n values are $\dot{M} \approx 5\,(0.6) \times 10^{-6}(v_w/10\,\mathrm{km\,s^{-1}})^{-1}\,M_\odot\,\mathrm{yr}^{-1}$ for $n = 8$ (9) and $\dot{M} < 10^{-7}(v_w/10\,\mathrm{km\,s^{-1}})^{-1}\,M_\odot\,\mathrm{yr}^{-1}$ for $n \geqslant 10$.

To model the radio emission from the interaction between the ejecta and the circumstellar medium, we use the similarity solutions and methods of Chevalier (1982) and Chevalier & Fransson (2017). The propagation of the radius of the interaction region $R_s \propto t^{(n-3)/(n-2)}$, and we assume that the fraction ϵ_B of the forward shock energy density $\rho_w V_s^2$ goes into the magnetic field energy density and that the fraction ϵ_e goes into the relativistic electron energy density. For the relativistic electrons, we assume a power-law distribution of the electron energies, $dN/dE = N_0 E^{-p}$, where $E = \gamma m_e c^2$ is the energy of the electrons, and γ is the Lorentz factor. The intensity of the

optically thin synchrotron emission is then $\propto \nu^{-\alpha}$, where $\alpha = (p-1)/2$. We have used $p = 3$. The volume of the region that generates synchrotron emission is assumed to be the entire volume between the forward shock and the contact discontinuity between the shocked ejecta and shocked circumstellar gas. The synchrotron emission suffers from both SSA and external FFA. A crucial parameter for FFA is the temperature of the circumstellar gas, which is uncertain (e.g., Lundqvist & Fransson 1988). We have used 5×10^4 K. We have also assumed the H and He in the circumstellar gas to be fully ionized, which may overestimate the degree of ionization for an LL Type IIP. With these assumptions, we show in Figure 4 the modeled radio emission (with and without FFA) for a model with $n = 9.2$, $\epsilon_B = 0.01$, and $\epsilon_e = 0.1$. The mass-loss rate is $5 \times 10^{-7}(v_w/10\,\mathrm{km\,s^{-1}})^{-1}\,M_\odot\,\mathrm{yr}^{-1}$. For this and smaller values of $\dot{M}/v_w$, the modeled radio fluxes are lower than the observed upper limits, and FFA is less important than SSA at the peak fluxes of each observed frequency. It is also obvious that at the epoch of the LOFAR observations, the modeled flux is about 2 orders of magnitude below the detection limit. In the $n = 9.2$ model, the maximum velocity of the unshocked ejecta at this epoch is $\sim$4060 km s^{-1}, which is too slow to generate any appreciable synchrotron emission. It is also possible to avoid radio detection for very dense winds, since FFA will then operate efficiently and make radio emission nondetectable. To estimate the lowest mass-loss rate needed for this to happen, we have run models with $\epsilon_B = \epsilon_e = 0.1$ and $a = 0$ and found that no emission would be detected for models with $n \leqslant 6.6$, which all have $\dot{M} \geqslant 8.5 \times 10^{-5}(v_w/10\,\mathrm{km\,s^{-1}})^{-1}\,M_\odot\,\mathrm{yr}^{-1}$, with the 150 MHz observations being decisive. We have included a model with $n = 6.6$ and $\dot{M} = 8.5 \times 10^{-5}(v_w/10\,\mathrm{km\,s^{-1}})^{-1}\,M_\odot\,\mathrm{yr}^{-1}$ in Figure 4. We find this scenario to avoid radio detection less

likely because $\tau_e \geqslant 50$ (for fully ionized ejecta) at 20 days in these models, which would require an electron fraction in the ejecta at 20 days, which is less than ~ 0.01 to be compatible with the results of Kozyreva et al. (2022). Moreover, such a dense wind may produce narrow circumstellar spectral lines that are not detected, hence eliminating such a scenario. If we had assumed $\epsilon_B = 0.01$, as for the SSA-dominated models in Figure 4, the wind density would have been even more extreme.

To obtain a detectable 150 MHz signal at 6428 days without producing detected emission at higher frequencies during early epochs, the circumstellar medium could be dilute close to the SN and denser at larger radii. Figure 4 includes the 150 MHz light curve for such a circumstellar "shell" model. Here we have assumed that the maximum ejecta speed is ~ 9600 km s^{-1} at ~ 3900 days when the circumstellar shock runs into a shell characterized by the progenitor mass-loss rate $\dot{M} \approx 1.8 \times 10^{-6}(v_w/10\ \mathrm{km\ s^{-1}})^{-1}\ M_\odot\ \mathrm{yr}^{-1}$. (This means that we have assumed almost no deceleration of the outermost ejecta until they enter the region of increased circumstellar density.) The parameters are otherwise the same as for the other $n = 9.2$ model in Figure 4 (i.e., $n = 9.2$, $\epsilon_B = 0.01$, and $\epsilon_e = 0.1$). The inner radius of increased circumstellar density is 4×10^{17} cm. Since it takes a few expansion timescales to set up a similarity solution, we have scaled the flux with the swept-up mass because the shock crossed 4×10^{17} cm compared to the swept-up mass for a "mature" similarity solution. The swept-up mass scales linearly with radius for a $\rho_w \propto r^{-2}$ wind, so the scaling factor is simply $1 - (4 \times 10^{17}/R_s)$. (For a more detailed discussion of shell interaction and how quickly a similarity solution is obtained, see Harris et al. 2016.) At 6428 days, the circumstellar shock is at 6.2×10^{17} cm, and the swept-up mass of the high-density region is $\sim 0.013\ M_\odot$. This gives a rough estimate of how the LOFAR observation constrains a possible high-density shell at these radii.

The results in Figure 4 were derived for $\epsilon_e = 0.1$ and $\epsilon_B = [0.01, 0.1]$. These values are often used to estimate $\dot{M}/v_w$ for radio SNe (e.g., Lundqvist et al. 2020), and within this range of values for ϵ_B, we used $\epsilon_B = 0.01$ to obtain the highest possible upper limit of $\dot{M}/v_w$ in the SSA-dominated case. For the FFA-dominated case, we used ϵ_B to get the lowest possible lower limit of $\dot{M}/v_w$. However, we emphasize that there is considerable uncertainty in the values for ϵ_B and ϵ_e. In a recent investigation, Reynolds et al. (2021) found that $0.001 \lesssim \epsilon_B \lesssim 0.1$ and $10^{-4} \lesssim \epsilon_e \lesssim 0.05$ for six young SN remnants, and that there are variations of ϵ_B and ϵ_e even within the same remnant. If we include this information, it will not affect the lowest possible lower limit in the FFA-dominated case for SN 2005cs in Figure 4 (since this was estimated from large values of ϵ_e and ϵ_B), but it will affect the highest possible upper limit of $\dot{M}/v_w$ in the SSA-dominated case. If we fix ϵ_B at $\epsilon_B = 0.1$ and set $\epsilon_e = 0.05\ (0.001, 2 \times 10^{-4})$, then the upper limit of $\dot{M}$ becomes $\dot{M} \lesssim 2\ (17, 390) \times 10^{-7}(v_w/10\ \mathrm{km\ s^{-1}})^{-1}\ M_\odot\ \mathrm{yr}^{-1}$ for $n = 9.5\ (8.5, 7.0)$ and $a = 0$. For $\epsilon_e = 10^{-4}$, there is no solution for $n \geqslant 6$. However, if we only allow $n \geqslant 8$ (cf. above), the smallest possible value for ϵ_e is 3×10^{-4}, for which $\dot{M} \lesssim 5 \times 10^{-6}(v_w/10\ \mathrm{km\ s^{-1}})^{-1}\ M_\odot\ \mathrm{yr}^{-1}$. We can also fix ϵ_e at $\epsilon_e = 0.05$ and set $\epsilon_B = 0.1\ (0.01, 0.001)$. We then find $\dot{M} \lesssim 2\ (7, 26) \times 10^{-7}(v_w/10\ \mathrm{km\ s^{-1}})^{-1}\ M_\odot\ \mathrm{yr}^{-1}$ for $n = 9.5\ (8.9, 8.3)$ and $a = 0$. In all models with $\dot{M} \gtrsim 10^{-6}(v_w/10\ \mathrm{km\ s^{-1}})^{-1} M_\odot\ \mathrm{yr}^{-1}$, FFA also starts to become important for the SSA-dominated case.

In summary, due to the unknown values of ϵ_e and ϵ_B, there is considerable uncertainty about the highest possible upper limit of $\dot{M}/v_w$ in the SSA-dominated case. However, looking at other SNe IIP, there are hints of deviation from energy equipartition between relativistic electrons and magnetic field strength with $\alpha \sim 10$–100, and the derived mass-loss rates are in the range $\dot{M} \sim (1 - 10) \times 10^{-6}(v_w/10\ \mathrm{km\ s^{-1}})^{-1}\ M_\odot\ \mathrm{yr}^{-1}$ (e.g., Ruiz-Carmona et al. 2022, and references therein). If we assume $\epsilon_e = 0.05$ and $\alpha = 30$, i.e., $\epsilon_B = 0.0017$ for SN 2005cs, we obtain an upper limit of $\dot{M} \lesssim 1.7 \times 10^{-6}(v_w/10\ \mathrm{km\ s^{-1}})^{-1}\ M_\odot\ \mathrm{yr}^{-1}$ (for $n = 8.5$ and $a = 0$), which could argue for the progenitor of SN 2005cs having somewhat less mass loss than for the average SN IIP, unless $\epsilon_e = 0.05$ and $\alpha \gtrsim 100$. For the same reasons, the limit on $\dot{M}$ characterizing a high-density shell probed by the LOFAR data is higher if we allow for lower values of ϵ_e and ϵ_B. In this case, the limit for such a shell is instead $\dot{M} \lesssim 6 \times 10^{-6}(v_w/10\ \mathrm{km\ s^{-1}})^{-1}\ M_\odot\ \mathrm{yr}^{-1}$ for $n = 8.5$, $a = 0$, $\epsilon_e = 0.05$, and $\alpha = 30$.

3.2. M51a AGN-related Sources

The morphology of the radio nuclear emission from the center of M51 in the ILT image (Figure 5) is similar to the morphology seen in other radio studies by, e.g., Maddox et al. (2007) and Dumas et al. (2011) using the VLA, with the AGN core in the center, the extranuclear cloud (XNC) to the south, and ringlike emission from the northern bubble above. However, while the VLA observations only show a compact source at the center, the radio morphology seen in the ILT image is a narrow, elongated structure toward the south like the EVN image in Rampadarath et al. (2015), albeit without resolving the subcomponents in the AGN core. The position of the AGN (Table 1) agrees well with the position reported by Rampadarath et al. (2015). Since the AGN core is unresolved, we cannot describe the subcomponents in detail as described by Rampadarath et al. (2015), but the PYBDSF fit for the AGN core is given in Table 1 (source 1).

The XNC morphology is similar to the one described by Crane & van der Hulst (1992), with a thin jet connecting the AGN to the XNC. They also described a bow shock in the XNC from the interaction of the jet with the surrounding interstellar medium, which seems likely from the ILT image as well. Bradley et al. (2004) and Ford et al. (1985) also suggested continuous fueling of the XNC by the jet. We estimate a flux density of 71.45 ± 3.00 mJy for the XNC using the task IMSTAT in CASA.

The ILT image also shows the northern bubble that is thought to be blown out due to an earlier ejection cycle from the AGN (Maddox et al. 2007). It is similar to the structure reported by them indicating cooler gas within. For the northern bubble, since PYBDSF does not pick up emission from the entire region, we estimate a flux density of 131.44 ± 0.12 mJy using the task IMSTAT in CASA.

In addition, we also detect extended emission coincident with the position of Component N. It is possible that our image at 145 MHz has almost resolved out emission from Component N and can only faintly detect extended emission at this resolution unlike a compact source. We also convolved the image with a bigger beam of $1.''08 \times 1.''02$ (similar to the VLA-A 20 cm image in Rampadarath et al. 2015) and compared it with the 6$''$ LoTSS image. Even when convolved with a bigger beam, the source remains extended and is spread over an area of about 15$''$. We estimate a flux density of 55.08 ± 8.08 mJy
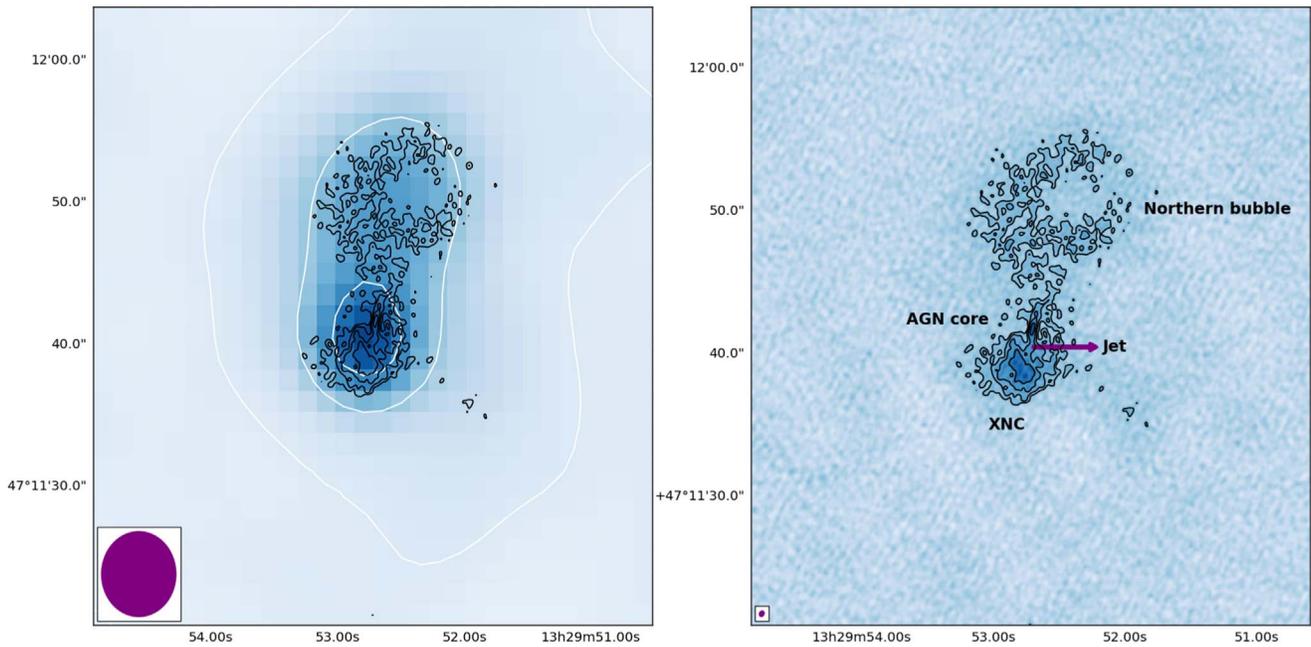
Figure 5. Left: ILT image of the center of M51 in black contours overlaid on the LoTSS 6″ resolution image in the background in white contours. Contours are from 2σ to 5σ for the ILT and 1σ to 5σ for LoTSS. Right: the ILT image is in the background and also in the black contours overlaid, with a linear stretch from -5σ to $+5\sigma$. The restoring beams for the two LOFAR images are shown in the bottom left corners.

using IMSTAT in CASA (this flux density matches what is estimated by PYBDSF at the same position with a source size of $34'' \times 17''$). Given that we do not detect a compact source, we do not include Component N in the source list. Rampadarath et al. (2015) suggested a study of the synchrotron aging of Component N, as discussed in Condon et al. (1991). However, we see no evidence of a break frequency in the VLA data in the literature; therefore, we do not see evidence of synchrotron aging in Component N. Also, if the emission we detect at the position of Component N truly comes from it, as is most likely the case, then there is no absorption at LOFAR frequencies. We therefore conclude that Component N may indeed be a fossil radio hot spot that has left behind a diffuse shell from the loss of continuous energy from the AGN, as suggested by Rampadarath et al. (2015).

3.3. Other Sources and Their Identifications

First, a note on detecting H II regions: from Equation (5) in Condon et al. (1991) and using the M51 ILT image, for a beam size of $\theta_M = 0.''436$, $\theta_m = 0.''366$ and a flux density detection limit of 5×0.046 mJy, the lower limit of the brightness temperature for compact sources detected at 145 MHz is $10^{4.9}$ K. Free–free emissions from H II regions have brightness temperatures up to 2×10^4 K (Wilson et al. 2009). Hence, as first noted in Varenius et al. (2015), the resolution of the ILT image rules out any of the detected objects being H II regions. Hence, the candidates for the sources detected in this ILT image of M51 are expected to be background sources, AGNs, high-mass X-ray binaries, and SN remnants.

3.3.1. J133005+471035

Source 3 in Table 1, J133005+471035, is resolved into four components with the EVN and compact with the VLA (Rampadarath et al. 2015). With the ILT, it is not fully resolved, but it clearly is not a single compact structure either.

Rampadarath et al. (2015) concluded that a two-sided jet from an active nucleus is a possible scenario from their EVN image.

3.3.2. [MZF2015] J1329+4717

Source 8 in Table 1 is a bright radio source visible in both LoTSS (compact) and ILT (extended emission with two apparent lobes). The VLA data from Mao et al. (2015) classify it as an extragalactic background radio source.

3.3.3. M51b

Source 9 in Table 1 is the interacting companion to M51a. A bright compact source in LoTSS, M51b shows extended resolved emission with the ILT.

3.3.4. J133016+471024

Source 10 in Table 1, J133016+471024, is a single bright source in LoTSS, whereas with the ILT, two lobes of extended emission are visible but not a central engine. (Hence, there was no cross-match with LoTSS for this particular source.) MERLIN and EVN images in Rampadarath et al. (2015) detect the unresolved central source, while the 20 cm VLA image shows a central source with two radio lobes with its morphology and luminosity placing it as a radio-loud AGN, an FR II galaxy.

3.3.5. CXOU J132954.9+470922

Source 11 in Table 1 is a high-mass X-ray binary. The source is not detected by LoTSS but has a high flux density similar to SN 2011dh and can be cross-matched with the NASA/IPAC Extragalactic Database. Maddox et al. (2007) found a spectral index of -0.3 for this source (listed as 65 in Table 2 of their work). The 20 cm flux density in their work can be extrapolated to 145 MHz (817 μJy), which matches very well with our finding of 830 μJy from PYBDSF.

4. Conclusion

This paper presents the first subarcsecond-resolution ILT image of the nearby galaxy M51 at 145 MHz. We discuss the compact sources in the galaxy, the center of M51, and the supernovae (SNe) in the galaxy. We detect SN 2011dh with the ILT, which is also seen in the LoTSS catalog. Importantly, we find that the LoTSS flux density for the SN is about five times higher than the flux density with our ILT image, which would affect the absorption scenario for the SN and, consequently, the mass-loss rates and other parameters. Using VLA and GMRT data at two different epochs combined with the ILT flux density, we derive the radii of the forward shock, the magnetic field strengths of the shocked circumstellar medium, and the corresponding mass-loss rates for the progenitor at these two epochs. The time evolution of the shock characterized by the parameter m seems consistent with previous studies. Our analysis also indicates that the mass-loss rate of the progenitor was higher just prior to the explosion or that the values for one or both of the ϵ parameters changed as the circumstellar shock evolved.

We do not detect SN 1994I or SN 2005cs, but we discuss both at some length, the former from extrapolated expected flux densities and the latter for the early-time light curves in light of a new explosion model. For SN 1994I, we find that the upper limit we obtain on the flux density at 7466 days with the ILT could be inconsistent with a scenario of constant mass-loss rate or could indicate weakening of the reverse shock. For SN 2005cs, we find that along with the upper limits on flux density at late times from the ILT image, the early radio data for the SN are consistent with the explosion model presented in Kozyreva et al. (2022) and an upper limit on the progenitor mass loss of $\dot{M} \lesssim$ few $\times$ $10^{-6} (v_w/10 \text{ km s}^{-1})^{-1} M_\odot \text{ yr}^{-1}$, with no possibility of the ejecta running into a shell. This is constrained by the lack of any detectable signal at 6428 days with the ILT, for which the ejecta would have to run into a high-density shell characterized by the progenitor mass-loss rate $\dot{M} \gtrsim 10^{-5} (v_w/10 \text{ km s}^{-1})^{-1} M_\odot \text{ yr}^{-1}$ to be detected.

We find that the morphology of the nuclear emission in M51 with the ILT is very similar to the morphology seen in the higher-frequency VLA by other studies. With the ILT, we are unable to fully resolve the AGN core, although it is not a compact source but rather narrow and elongated toward the XNC in the south. We also discuss the emission from the XNC (with a thin jet connecting the AGN and the XNC signaling continuous fueling of the XNC) and the northern bubble (with the same bubble structure that is visible at higher frequencies denoting cooler gas inside and the possibility of it being leftover from a previous ejection from the AGN), along with a possible detection of Component N (which we conclude may indeed be a fossil hot spot, with no evidence we can see of synchrotron aging at higher radio frequencies). We also present a few other interesting sources detected in the field with the ILT.

The results presented in this paper provide a proof of concept of the advantages of using the ILT to detect and characterize low-frequency radio emission from compact sources (including radio SNe) in nearby galaxies rather than relying on low $6''$ resolution LoTSS survey data using the Dutch baselines of LOFAR to study these objects. Going to higher angular resolution almost completely removes the effects of diffuse radio emission from the host galaxy, allowing more accurate flux density measurements, including accurate upper limits, to be made for such compact sources. In addition, our observations revealed two new compact sources in M51, which was not detected in low-resolution LoTSS images because it was too weak to be separated from the diffuse emission of the galaxy. It is interesting to note that if M51 was placed at even a slightly larger distance or the compact sources were slightly weaker in luminosity, then more compact sources, including SN 2011dh, would not have been detectable in the LoTSS $6''$ resolution images due to confusion with the diffuse galactic continuum. In contrast, these sources would still have been detectable using the ILT. This observation demonstrates the potential advantages for extragalactic compact source population studies of large-scale automated ILT processing toward nearby galaxies using the extensive archive of the long baseline that exists as part of the LoTSS.

ORCID iDs

Deepika Venkattu ⬤ https://orcid.org/0000-0001-9896-6994
Peter Lundqvist ⬤ https://orcid.org/0000-0002-3664-8082
Miguel Pérez Torres ⬤ https://orcid.org/0000-0001-5654-0266

Venkattu et al.

Leah Morabito ⓘ https://orcid.org/0000-0003-0487-6651
Javier Moldón ⓘ https://orcid.org/0000-0002-8079-7608
John Conway ⓘ https://orcid.org/0000-0003-2448-9181
Poonam Chandra ⓘ https://orcid.org/0000-0002-0844-6563

References

Astropy Collaboration, Price-Whelan, A. M., Lim, P. L., et al. 2022, ApJ, 935, 167
Björnsson, C. I. 2015, ApJ, 813, 43
Bradley, L. D., Kaiser, M. E., & Baan, W. A. 2004, ApJ, 603, 463
CASA Team, Bean, B., Bhatnagar, S., et al. 2022, PASP, 134, 114501
Chevalier, R. A. 1982, ApJ, 258, 790
Chevalier, R. A., & Fransson, C. 2017, in Handbook of Supernovae, ed. A. W. Alsabti & P. Murdin (Cham: Springer), 875
Condon, J. J. 1992, ARA&A, 30, 575
Condon, J. J., Huang, Z. P., Yin, Q. F., & Thuan, T. X. 1991, ApJ, 378, 65
Crane, P. C., & van der Hulst, J. M. 1992, AJ, 103, 1146
de Witt, A., Bietenholz, M. F., Kamble, A., et al. 2016, MNRAS, 455, 511
Dumas, G., Schinnerer, E., Tabatabaei, F. S., et al. 2011, AJ, 141, 41
Ergon, M., & Fransson, C. 2022, A&A, 666, A104
Ford, H. C., Crane, P. C., Jacoby, G. H., Lawrie, D. G., & van der Hulst, J. M. 1985, ApJ, 293, 132
Foreman-Mackey, D., Hogg, D. W., Lang, D., & Goodman, J. 2013, PASP, 125, 306
Griga, T., Marulla, A., Grenier, A., et al. 2011, CBET, 2736, 1
Harris, C. E., Nugent, P. E., & Kasen, D. N. 2016, ApJ, 823, 100
Harris, C. R., Millman, K. J., van der Walt, S. J., et al. 2020, Natur, 585, 357
Horesh, A., Stockdale, C., Fox, D. B., et al. 2013, MNRAS, 436, 1258
Hunter, J. D. 2007, CSE, 9, 90
Intema, H. T., Jagannathan, P., Mooley, K. P., & Frail, D. A. 2017, A&A, 598, A78
Jackson, N., Tagore, A., Deller, A., et al. 2016, A&A, 595, A86
Jackson, N., Badole, S., Morgan, J., et al. 2022, A&A, 658, A2
Kloehr, W., Muendlein, R., Li, W., Yamaoka, H., & Itagaki, K. 2005, IAU Circ., 8553, 1
Kowal, C. T., & Sargent, W. L. W. 1971, AJ, 76, 756
Kozyreva, A., Janka, H.-T., Kresse, D., Taubenberger, S., & Baklanov, P. 2022, MNRAS, 514, 4173
Krauss, M. I., Soderberg, A. M., Chomiuk, L., et al. 2012, ApJL, 750, L40
Kukreti, P., Morganti, R., Shimwell, T. W., et al. 2022, A&A, 658, A6
Kundu, E., Lundqvist, P., Sorokina, E., et al. 2019, ApJ, 875, 17
Lebigot, E. O. 2010

Lundqvist, P., & Fransson, C. 1988, A&A, 192, 221
Lundqvist, P., Kundu, E., Pérez-Torres, M. A., et al. 2020, ApJ, 890, 159
Maddox, L. A., Cowan, J. J., Kilgard, R. E., Schinnerer, E., & Stockdale, C. J. 2007, AJ, 133, 2559
Mao, S. A., Zweibel, E., Fletcher, A., Ott, J., & Tabatabaei, F. 2015, ApJ, 800, 92
Mohan N., & Rafferty D. (2015) PyBDSF: Python Blob Detection and Source Finder, Astrophysics Source Code Library ascl:1502.007
Morabito, L. K., Jackson, N. J., Mooney, S., et al. 2022, A&A, 658, A1
Offringa, A. R., & Smirnov, O. 2017, MNRAS, 471, 301
Offringa, A. R., McKinley, B., Hurley-Walker, N., et al. 2014, MNRAS, 444, 606
Pastorello, A., Sauer, D., Taubenberger, S., et al. 2006, MNRAS, 370, 1752
Polisensky, E., Lane, W. M., Hyman, S. D., et al. 2016, ApJ, 832, 60
Puckett, T., Armstrong, J., Johnson, W., et al. 1994, IAU Circ., 5961, 1
Ramírez-Olivencia, N., Varenius, E., Pérez-Torres, M., et al. 2022, A&A, 658, A4
Ramírez-Olivencia, N., Varenius, E., Pérez-Torres, M., et al. 2018, A&A, 610, L18
Rampadarath, H., Morgan, J. S., Soria, R., et al. 2015, MNRAS, 452, 32
Reynolds, S. P., Williams, B. J., Borkowski, K. J., & Long, K. S. 2021, ApJ, 917, 55
Roy, S., & Manna, S. 2021, MNRAS, 507, 4734
Ruiz-Carmona, R., Sfaradi, I., & Horesh, A. 2022, A&A, 666, A82
Shimwell, T. W., Tasse, C., Hardcastle, M. J., et al. 2019, A&A, 622, A1
Shimwell, T. W., Hardcastle, M. J., Tasse, C., et al. 2022, A&A, 659, A1
Stockdale, C. J., Kelley, M., van Dyk, S. D., et al. 2005, IAU Circ., 8603, 2
Tabatabaei, F. S., Schinnerer, E., Krause, M., et al. 2017, ApJ, 836, 185
Timmerman, R., van Weeren, R. J., Callingham, J. R., et al. 2022, A&A, 658, A5
van Diepen G., Dijkema T. J., & Offringa A. (2018) DPPP: Default Pre-Processing Pipeline, Astrophysics Source Code Library ascl:1804.003
van Haarlem, M. P., Wise, M. W., Gunst, A. W., et al. 2013, A&A, 556, A2
van Weeren, R. J., Shimwell, T. W., Botteon, A., et al. 2021, A&A, 651, A115
Varenius, E., Conway, J. E., Martí-Vidal, I., et al. 2015, A&A, 574, A114
Varenius, E., Conway, J. E., Martí-Vidal, I., et al. 2016, A&A, 593, A86
Vinkó, J., Takáts, K., Szalai, T., et al. 2012, A&A, 540, A93
Virtanen, P., Gommers, R., Oliphant, T. E., et al. 2020, NatMe, 17, 261
Weiler, K. W., Panagia, N., Stockdale, C., et al. 2011, ApJ, 740, 79
Wilson, T. L., Rohlfs, K., & Hüttemeister, S. 2009, Tools of Radio Astronomy (Berlin: Springer)
Winkler, P. F., Coffin, S. C., Blair, W. P., Long, K. S., & Kuntz, K. D. 2021, ApJ, 908, 80
Yadav, N., Ray, A., & Chakraborti, S. 2016, MNRAS, 459, 595